Toward durable protonic ceramic cells: Hydration-induced chemical expansion correlates with symmetry in the Y-doped BaZrO₃ – BaCeO₃ solid solution

Ting Chen^{$l,2\S^{\circ}$}, Yuhang Jing^{$3\S^{\circ}$}, Lawrence O. Anderson^{$4,5\S$}, Kwati Leonard^{$l\S$}, Hiroshige Matsumoto^l, Narayana Aluru^{3°}, and Nicola H. Perry^{4,5,1*}

- ¹ International Institute for Carbon-Neutral Energy Research, Kyushu University, 744 Motooka, Nishi-ku Fukuoka, 819-0395 Japan
- ² Department of Hydrogen Energy Systems, Kyushu University, 744 Motooka, Nishi-ku Fukuoka 819-0395, Japan
- ³ Department of Mechanical Science and Engineering, University of Illinois at Urbana-Champaign, 1206 W. Green St., Urbana, IL 61801 U.S.A.
- ⁴ Department of Materials Science and Engineering, University of Illinois at Urbana-Champaign, 1304 W Green St., Urbana, IL, 61801 U.S.A.
- ⁵ Materials Research Laboratory, University of Illinois at Urbana-Champaign, 104 S. Goodwin Ave., Urbana IL, 61801, U.S.A.

ABSTRACT

Electrolytes and electrodes in protonic ceramic electrolysis/fuel cells (PCECs/PCFCs) can exhibit significant chemical strains upon incorporating H_2O into the lattice. To increase PCEC/PCFC durability, oxides with lower hydration coefficients of chemical expansion (CCEs) are desired. We hypothesized that lowering symmetry in perovskite-structured proton conductors would lower their CCEs and thus systematically varied the tolerance factor through B-site substitution in the prototypical $BaCe_{0.9-x}Zr_xY_{0.1}O_{3-\delta}$ ($0 \le x \le 0.9$) solid-solution. X-ray diffraction (XRD) confirmed symmetry decreased with decreasing Zr content. CCEs were measured by isothermal XRD, dilatometry, and thermogravimetric analysis (TGA) in varied pH₂O over 430-630 °C. With decreasing Zr content, isothermal H_2O uptake was greater, but corresponding chemical strains were smaller; therefore, CCEs monotonically decreased. Density functional theory simulations on endmember $BaCe_{1-y}Y_yO_{3-\delta}$ and $BaZr_{1-y}Y_yO_{3-\delta}$ compositions showed the same trend. Lower CCEs

in this solid solution correlate to decreasing symmetry, increasing unit cell volume, increasing oxygen vacancy radius, decreasing bulk modulus, and inter- vs. intra-octahedral hydrogen bonding. Microstructural constraints may also contribute to lower macroscopic CCEs in lower symmetry bulk ceramics, based on observed anisotropic chemical expansion and enhanced strains in powder vs. bulk BaCe_{0.9}Y_{0.1}O_{3-δ}. The results inform design principles for rational tailoring of CCEs and materials choice for chemo-mechanically durable devices.

KEYWORDS

Proton conductor; chemical expansion; hydration; tolerance factor; strain; perovskites

1. INTRODUCTION

Electrochemical devices, such as fuel/electrolysis cells, are integral components of a sustainable energy infrastructure^{1,2}. Fuel cells can efficiently derive electrical power and heat from air and a variety of fuels, while their reverse operation as electrolysis cells provides a means to store electrical energy as chemical fuel. Typically, solid oxide fuel/electrolysis cells operate at high temperatures (600-1000 °C), while proton-exchange membrane or polymer electrolyte membrane cells operate at low temperatures (25-100 °C). Bridging these two typical temperature ranges to work in the intermediate temperature range (~400-600 °C) has the potential to combine some of the benefits of both low and high temperature operation – high efficiency, no precious metal catalysts, and fuel flexibility (high temperature) plus short start-up times, low cost interconnect materials, and high durability (low temperature). In order to operate solid oxide cells at intermediate temperatures, materials with high ionic conductivity and low electronic conductivity are needed for the electrolyte layer. Certain proton conducting oxides offer higher ionic conductivity^{3–5} than the best oxide ion conductors (acceptor-stabilized ZrO₂, acceptor-doped

CeO₂, and Sr- and Mg- codoped LaGaO₃) and so can operate at lower temperatures with the same Ohmic resistance for an equivalent electrolyte geometry. Additionally, electrolysis cells using proton-conducting electrolytes generate H₂ at the fuel electrode that is undiluted with H₂O, and proton conductors are also under development for gas separation and electrochemical reactors^{5–9}. Among proton conductors, the Y-doped BaZrO₃-BaCeO₃ solid solution has received significant attention. The wide bandgap zirconate endmember offers high ionic conductivity and stability but is challenging to sinter to full density leading to high grain boundary electrical resistance^{10–12}, while the cerate endmember offers greater ease in processing, higher proton content at elevated temperatures, and lower hole transference numbers¹³, but with less tolerance for humid, CO₂ containing environments¹⁴ and higher n-type electronic conductivity under reducing conditions^{15,16}. Intermediate compositions provide a compromise between the strengths and weaknesses of the endmembers, with BaZr_{0.7}Ce_{0.2}Y_{0.1}O_{3-δ} being a composition of choice in some studies^{17,18}.

In addition to transporting protons through the lattice, these acceptor-doped materials can also exchange H₂O with the surrounding gas environment, as described in eq. 1.

$$v_0^{\bullet\bullet} + 0_0^{\times} + H_2 0 \leftrightarrow 2(0H)_0^{\bullet} \tag{1}$$

Here, water from the gas phase dissociates as it enters the ceramic lattice, filling an oxygen vacancy and inserting H species. The O and H ions are often denoted as effectively sharing an oxygen site, via the (OH)*O Kroger-Vink notation. Reaction 1 is valid for operation in a condition where concurrent redox reactions, enabling the hydrogenation processes 19–22 shown in eq. 2, are deemed insignificant, e.g., due to the negligible concentration of electronic defects in the measurement conditions relative to oxygen vacancies. (The hydrogenation process on the left is for a p-type

system, while the hypothetical reaction on the right is for an n-type system, which is not typically reported in this context.)

$$H_2O + 2O_0^{\times} + 2h^{\bullet} \rightarrow 2(OH)_0^{\bullet} + \frac{1}{2}O_2(g)$$
 or $H_2O + 2O_0^{\times} \rightarrow 2(OH)_0^{\bullet} + \frac{1}{2}O_2(g) + 2e'$
(2)

The pure hydration process in eq. 1, which is studied in the present work, is accompanied by a distortion in the lattice, termed chemical strain or chemical expansion, with significant implications for device mechanical integrity. Phenomenologically, the linear chemical strain (ε_c) is often found to be proportional to the change in defect concentration ($\Delta[(OH)_O^{\bullet}]$) for the hydration reaction, with units of concentration per formula unit) by the linear coefficient of chemical expansion (CCE), as shown in eq. 3:

$$CCE = \frac{\varepsilon_C}{\Delta \left[(OH)_O^{\bullet} \right]} \tag{3}$$

Macroscopically, in randomly oriented polycrystalline materials the scalar treatment of the CCE is appropriate. At an atomistic scale, simulations have represented chemical expansion by point defect-induced strain tensors with locally anisotropic behavior possible even in nominally cubic systems^{23,24}. In non-cubic systems, anisotropic strains can be observed on a single crystal or local grain level^{25–27}. In such cases the volumetric chemical expansivity would be the sum of the linear CCEs along the three orthogonal directions. The chemical stress associated with all these chemical strains can be large enough to cause mechanical failure such as cracking and delamination within devices where components are constrained and/or experiencing non-uniform defect concentrations^{28,29}. This effect can be particularly pronounced in proton conductors, compared to oxygen loss in mixed oxide ion and electronic conductors, as hydration-induced lattice strains of

up to 1% have been reported^{30,31}. Therefore, there is interest in quantifying CCEs for the purposes of device design and modeling as well as in understanding chemical and structural design rules for rationally tailoring CCEs to optimize components' chemo-mechanical response.

Several groups have reported observations of hydration-induced chemical expansion in acceptor-doped BaZrO₃-BaCeO₃³²⁻³⁵. Computationally, DFT simulations have modeled the size and shape of point defects involved in the hydration process, as in eq. 1. Jedvik et al. have shown that oxygen vacancies $(v_0^{\bullet\bullet})$ are smaller than $(OH)_0^{\bullet}$ defects, which are smaller than oxide ions O_0^{x} . In this case, the chemical expansion process may be a competition between a slight contraction induced by replacing O_0^x with $(OH)_0^{\bullet}$ and a larger expansion induced by replacing $V_0^{\bullet \bullet}$ with $(OH)_0^{\bullet}$. Experimentally, with the exception of a macroscopic study by Kreuer using dilatometry¹, most papers on proton conductors report chemical strains at the unit cell level measured by in situ Xray or neutron diffraction ^{30,31,36,37}. Although diffraction enables insight into strain anisotropy, the common non-isothermal methodology has not leant itself well to accurate, quantitative determination of hydration CCEs. Typically, lattice parameters vs. temperature are measured while heating and cooling^{31,37,38}, during which process the hydration degree varies, leading to deviations from conventional thermal expansion behavior; i.e., the total strain is a superposition of thermal and chemical contributions. If the measurements are performed in a single gas atmosphere, i.e., one humidity, chemical strains at a given temperature can arise from hysteresis in hydration degree during heating vs. cooling. In this case, the strains are measured in a non-equilibrium condition, and non-uniform proton concentrations throughout the material in such cases may result in peak broadening or asymmetry. Chemical strains can also be measured in equilibrium conditions by repeating a temperature excursion in different gas atmospheres, i.e., different H₂O contents, and dwelling at each temperature point until steady-state behavior is obtained. It should be noted that these variable temperature approaches typically assume that the thermal expansion contribution is constant, regardless of hydration degree; however, a recent study has shown that (isostoichiometric) coefficients of thermal expansion are hydration-dependent³⁴. This means that hysteretic differences in strain during heating vs. cooling, or equilibrium strain differences in different humidities, may be attributable to changes in thermal strain as well as chemical strain, even though they have been attributed to solely chemical strain in previous studies. Such non-isothermal measurements also assume that redox processes during heating and cooling are negligible³⁹, which may not be the case, depending on oxygen partial pressure and temperature. In the present work we instead pursue an isothermal approach that enables isolation of chemical strain from any thermal effects, in equilibrium (uniform proton concentration), absent of significant redox contributions.

In order to determine CCEs, the changes in proton concentration must be measured under identical conditions to the measured chemical strains. Therefore, isothermal comparisons in different humidities (keeping the oxygen partial pressure constant at an intermediate value) are preferred. Generally, such direct comparisons of strain and quantified proton content change have not yet been made in the literature for all of these compositions. Reported hydration-induced chemical strains for this solid solution (typically in the temperature range 300-600 °C) range from 0.03^{40} to $0.5\%^{32}$ and, for Y-doped BaZrO₃, increase with increasing acceptor dopant concentration, as expected from eq. 1, because the change in proton concentration can be greater when more oxygen vacancies are stabilized in the structure. Reported CCEs for this solid solution range over an order of magnitude with values as low as 0.006^{40} , but often, the changes in proton concentration were assumed to represent full hydration/dehydration, rather than measured, likely leading to some CCE under-estimations. Even in the rare cases with the proton concentration change measured at

isolated temperature points, there is considerable variation⁴¹, with reported CCEs varying by a factor of 5 for BaCeO₃ materials^{31,42} (~0.01-0.05 CCE estimated from volumetric chemical expansivity) and by at least a factor of 2 for BaZrO₃ materials³² (~0.045-0.09 CCE estimated from volumetric chemical expansivity) depending on Y content.

In this work, we seek to provide macroscopic CCE values over a range of practical application temperatures, by measuring isothermal chemical strains by dilatometry and XRD and associated isothermal proton concentration changes by thermogravimetric analysis under identical partial pressures of H₂O and ensuring attainment of steady-state conditions. Further, by studying 4 compositions systematically across the solid solution, by both in situ characterization and density functional theory simulation, we aim to uncover and understand, on a structural and chemical basis, the trends in CCE. Our initial hypothesis was that perovskite proton conductors with increasing crystallographic distortions (lower symmetry) vs. cubic perovskites would exhibit decreasing CCEs. In this solid solution, we can systematically vary the A:B site average cation size ratio, in order to induce crystallographic distortions leading to different symmetries, as predicted by a tolerance factor analysis. At a crystal chemical level, we consider that distorted perovskites may accommodate chemical stresses through facile changes in their octahedral tilts/rotations; such changes would lengthen some bonds and shorten others, so that one expects only small overall lattice volume changes. As a result of the reduced symmetry (vs. cubic perovskites), we expect that distorted perovskites will exhibit anisotropic chemical expansion, as has been observed before for other compositions^{25,27,43–45}. At a macroscopic level, in polycrystalline bulk ceramics with randomly oriented grains, this anisotropy may lead to a) averaging of linear chemical strains in any given direction and b) constraining of the strain from adjacent grains – both effects potentially lowering CCEs in addition to any crystal chemical effects. The latter effect (b) would be less

apparent in unconstrained powders. In the description that follows, we present our experimental and computational results clarifying the CCE trend in the cerate-zirconate solid solution and its correlation to various structural features including symmetry.

2. APPROACH

2.1. Experimental Approach

2.1.1. Fabrication

Powders of BaZr_{0.9}Y_{0.1}O_{3- δ} (x=0.9), BaZr_{0.6}Ce_{0.3}Y_{0.1}O_{3- δ} (x=0.6), BaZr_{0.3}Ce_{0.6}Y_{0.1}O_{3- δ} (x=0.3), and BaCe_{0.9}Y_{0.1}O_{3- δ} (x=0), were synthesized by a modified chemical solution route as described elsewhere 46, using analytic grade metal nitrates - Ba(NO₃)₂ (Wako, 99.9%), ZrO(NO₃)₂ (Aldrich, 99%), Ce(NO₃)₃·6H₂O (Kanto Chemical Co., INC 99.99%), and Y(NO₃)₃·6H₂O (Mitsuwa's Pure Chemicals, 99.9 %) - as raw materials. Stock solutions of the metal nitrates with concentrations determined by an inductively coupled plasma technique (ICP Shimadzu, ICPE-9000) were weighed and added into an aqueous solution sequentially with continuous stirring. EDTA (Dojindo, 99%) and citric acid (Wako, 99%) were then added as chelating agents with the molar ratio of total metal ions to EDTA and citric acid set at 1:1.5:1.5. Ammonium hydroxide solution (Chameleon Regent, 28.0 % NH₃ in H₂O) was added to promote the dissolution of EDTA and to adjust the pH to ~ 9 . The solution was then heated under stirring to evaporate water, until it changed into a viscous gel. The gel was then heat-treated at 240 °C in a vacuum oven to obtain a solid precursor which was calcined at 900 °C for 10 hours in air. The resulting powder was roll milled for 4 days to produce uniform, sub micrometer particles, which were dried. The obtained powders were pelletized with a Newton press and further compressed by cold isostatic pressing at 250 MPa. The compressed pellets were then sintered at 1400-1550 °C (higher temperature for Zrrich samples) for 10 h. Bars (\sim 22.5 mm x \sim 4 mm x \sim 3.5 mm) were cut from pellets using a diamond saw.

2.1.2. Characterization

Phase purity of the synthesized pellets was initially confirmed by X-ray diffraction (XRD Ultima IV) with Cu-K α radiation (40 kV, 40 mA). Diffraction patterns were obtained at room temperature in the 20 range between 10 ° and 80 ° with a step size of 0.02 °. Space group symmetry and lattice parameters were analyzed by pattern matching (PDFs 01-070-6747, 04-018-2314, 04-008-4455, and 04-020-2236 for x=0, 0.3, 0.6, and 0.9, respectively) and Rietveld refinement using HighScore software (Panalytical). Relative densities were estimated from geometric and mass measurements of dried samples. Tolerance factors were calculated using Shannon's ionic radii⁴⁷ from equation 4^{48} , where r_A , r_B , and r_X are the A-site, B-site, and anion radii, respectively:

$$t = \frac{r_A + r_X}{\sqrt{2}(r_B + r_X)} \quad (4)$$

Ionic radii values used were 1.61 Å (Ba²⁺ XII-fold coordinated), 0.9 Å (Y³⁺ VI), 0.72 Å (Zr⁴⁺ VI), 0.87 Å (Ce⁴⁺ VI), and 1.4 Å (O^{2-} VI).

Dilatometry was performed on the bar-shaped specimens using a lab-assembled single pushrod dilatometer to measure the expansion upon increasing the steam content in pure N₂ gas atmosphere at various temperatures in the range of 430-630 °C. Temperature was held constant in each case while the humidity was stepped to different values, and each humidity condition was held until the sample had reached a steady-state length. N₂ was selected to avoid high hole concentrations^{49,50}, which could be present in more oxidizing conditions, given the acceptor doping; similarly, highly reducing conditions were avoided to minimize the presence of Ce³⁺; these

constraints were chosen to limit the presence of the redox reactions shown in eq. 2^{49} . The steam content or pH₂O was controlled at 1.06% by bubbling the N₂ through water at 8 °C, with temperature controlled by a water bath (Multi Circulator MCX-250, AS ONE, Japan). No significant expansion was observed when the pH₂O was changed from ~1% to 20% at different values, therefore, pH₂O change from ~0% (UHP N₂ gas that has bypassed the water bath) to 1.06% was selected in this work. The corresponding isothermal changes of proton concentration (Δ [(OH)*o]) were measured by thermogravimetric analysis (TGA, lab assembled, using a Mettler-Toledo XP6 microbalance) under the same conditions as the dilatometry measurement, by evaluating the mass changes, according to eq. 5:

$$\Delta[(OH)_O] = \frac{\Delta m/MW_{OH}}{m_i/MW_{BCZY}}$$
(5)

where Δm is the isothermal mass change from ~0% to 1.06% pH₂O, m_i is the initial (dry) mass, and MW_x is the molecular weight of x. The pH₂O was also controlled by bubbling N₂ through water, with temperature controlled by a water bath. Owing to the possibility of sample mechanical failure during testing, which could influence dilatometric results, samples were analyzed by optical microscopy to check for the presence of any micro-cracks after the *in-situ* characterization. Additionally, several replicates of the x = 0 composition were tested with varying porosities, and in all cases, repeat measurements for hydration and dehydration in each condition were performed to check reversibility in both the TGA and dilatometry measurements.

In order to observe crystal structure as a function of temperature and humidity, to compare bulk vs. powder hydration strains, and to observe chemical strain anisotropy, *in situ*, high temperature XRD (HTXRD) was performed on the least symmetric (lowest tolerance factor) $BaCe_{0.9}Y_{0.1}O_{3-\delta}$ endmember. HTXRD was performed using the Bruker D8 Advance (Model # D8

Advance A25) with the Anton Paar HTK 1200N non-ambient stage and Dectris Eiger2R 500K detector, using Cu ka radiation with line focus, 60 mm Göbbel mirror and 0.2 mm divergence slit primary optics. A thermocouple in contact with the bottom of the sample stage monitored the sample temperature. In the temperature range where hydration is expected, i.e. 430-630°C, scans were taken with a 0.01° step size and 0.5 seconds/step over the 2θ range 25-90°. For all other temperatures, the scan rate was increased to 0.25 seconds/step. Scans were performed under the same conditions as the dilatometry and TGA measurements, except for the order of measurement: a series was first run in dry N₂, and then the measurements were repeated in N₂ with 1.06% H₂O. The powder sample was held at each temperature for 90 minutes prior to the XRD scan, and the measurements were made from high to low temperature steps in each case. Data were analyzed using pattern matching to ICSD structure files for BaCe_{0.9}Y_{0.1}O_{3-\delta} (Pnma #165828, Imma #193052, and $R\bar{3}c$ #193056) and Rietveld refinement with TOPAS (Bruker AXS, Version 6) software. Refinement parameters were added in the following sequence: 4th order Chebychev polynomial background, the appropriate structure file (lattice parameters), microstrain, sample displacement correction, and surface roughness correction. Near phase transitions, each structure file was fit individually, then together, to determine the contributions from each phase. Rwp values were less than 10% for all sample conditions.

2.2. Computational Approach

Density functional theory (DFT) calculations were performed with the projector augmented wave (PAW) method⁵¹ as implemented in the Vienna Ab initio simulation package (VASP)^{51–53}. The Perdew-Burke-Ernzerhof (PBE)⁵⁴ exchange-correlation functional was used. The cutoff energy for the plane wave basis set was 500 eV for all calculations. For improved accuracy, the pseudopotentials with valence states of Ba (5s, 5p, 6s), Zr (4s, 4p, 5s, 4d), Ce (5s,

5p, 6s, 5d, 4f), Y (4s, 4p, 5s, 4d), and O (2s, 2p) are chosen for all calculations. All atoms were relaxed by a conjugate gradient method until the forces on each atom were less than 0.02 eV/Å.

The orthorhombic bulk BaCeO₃ unit cell and cubic bulk BaZrO₃ unit cell were optimized using a 6×6×4 and 6×6×6 Monkhorst-Pack k-points mesh, respectively. The obtained lattice constants of orthorhombic BaCeO₃ unit cell (a=6.25 Å, b=6.26 Å, c=8.85 Å) and cubic BaZrO₃ unit cell (a=4.22 Å) are in good agreement with previous DFT and experimental results^{55,56}. Based on the optimized unit cell, a BaCeO₃ supercell with 2×2×2 orthorhombic unit cells and a BaZrO₃ supercell with 3×3×3 cubic unit cells were constructed and optimized. Next, one oxide ion vacancy was introduced in the supercells with two Zr or Ce ions substituted by two Y ions. The preferred positions of these two Y ions and the oxide ion vacancy were obtained through comparing the total energies of the system while locating them at different atomic sites. Finally, bulk Y-doped BaCeO₃ (BCY) and Y-doped BaZrO₃ (BZY) were obtained. A 2×2×2 Monkhorst-Pack k-points mesh was used for bulk calculations of BCY and BZY.

3. RESULTS

3.1. Experimental

Relative densities of the sintered samples were found to be 68 ± 6 %. The densities were intentionally kept below 100 % to facilitate faster kinetics of hydration/dehydration and attainment of equilibrium in each condition studied by TGA and dilatometry. (The hydration/dehydration kinetics in dense samples are expected to be limited by oxygen diffusion^{57,58}, which can be sluggish in the temperature range of this study.) This porosity could contribute to fracture during chemical expansion measurements^{59,60}, but post-analysis microscopy did not reveal the presence of cracks in the majority of samples. The x=0.6 sample exhibited some surface micro-cracks after analysis.

One x=0 sample broke during measurement and was not included in the analysis. Room temperature X-ray diffraction patterns of as-prepared samples are shown in Figure 1. Figure 1a shows the full range of 2θ values, confirming the perovskite structure with no significant secondary phase contributions for each sample, while Figure 1b shows an enlarged portion of the data in the 2θ range 28-31 degrees. Refinement of the patterns identified room temperature space group symmetries of cubic $Pm\bar{3}m$ for x=0.9, rhombohedral $R\bar{3}c$ for x=0.6 and 0.3 although

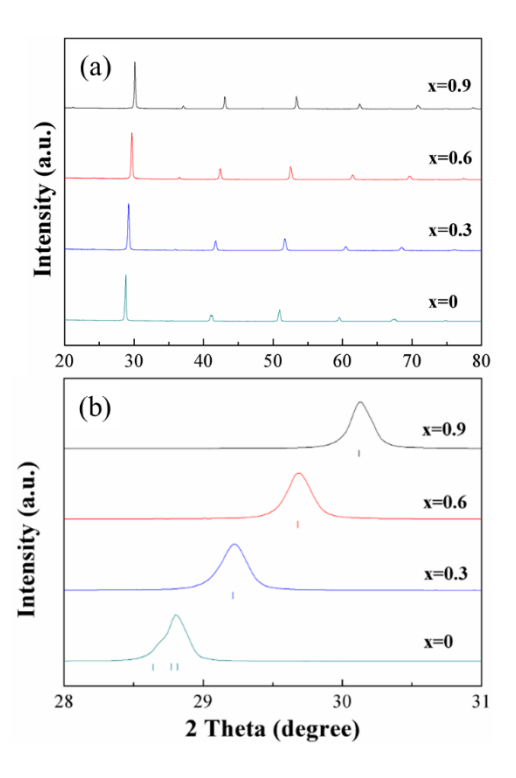


Figure 1. Room temperature X-ray diffraction patterns of the four compositions showing perovskite phase peaks (a) and a selection of the data (b) showing positional shift and distortion of most intense peak as Zr content (x) decreases. Indices from left to right are, Pnma (green): 200, 002, 121, $R\bar{3}c$ (blue and red): 110, 104, and $Pm\bar{3}m$ (black): 110.

x=0.6 was very close to $Pm\overline{3}m$ symmetry, and orthorhombic Pnma for x=0. The increasing distortion from cubic symmetry with decreasing x is consistent with the higher ionic radius of Ce vs. Zr and the corresponding decreasing calculated tolerance factors (eq. 1) of 0.996, 0.975, 0.955, and 0.936 for x=0.9, 0.6, 0.3, and 0, respectively. Substitution of the larger Ce for Zr also demonstrably increased the pseudo-cubic lattice parameter (a_{pc}) from 4.21 to 4.40 Å, determined

from fitting the XRD data for the actual lattice parameters and then calculating the equivalent cubic cell volumes. This trend is also visible in the shifting of peaks to lower angles with increasing Ce content in Figure 1b. These structural parameters are summarized, along with results discussed below, in Table 1.

Table 1. Selected measured properties for $BaCe_{0.9-x}Zr_xY_{0.1}O_{3-\delta}$ and calculated properties of $BaCe_{1-y}Y_yO_{3-\delta}$, and $BaZr_{1-y}Y_yO_{3-\delta}$

x	t	a _{pc} at 25 °C (Å)	Space group	CCE at 430 °C, measured	CCE at 630 °C, measured	CCE at 0 K, DFT
		[Y] = 0.06- 0.07				
0	0.936	4.40 (4.69 DFT at 0 K)	Pnma	0.00098	0.019	0.01269 (0.0122)
0.3	0.955	4.33	R3c	0.0015	0.019	
0.6	0.975	4.27	$R\overline{3}c$ (close to $Pm\overline{3}m$)	0.0091	0.023	
0.9	0.996	4.21 (4.24 DFT at 0 K)	Pm3̄m	0.028	0.049	0.02959 (0.01557)

Note: Simulated values in round parentheses are for a less-stable dopant configuration with distant Y dopants rather than the more stable configuration of closely spaced Y dopants used for the majority of the data.

From the dilatometry and TGA measurements, samples were observed to expand and gain mass upon increasing the H_2O content in the gas phase from ~ 0 to 1.06%, while keeping the pO_2 constant around 10^{-4} to 10^{-3} atm according to the sensor (using high purity N_2 gas). These transitions typically took place over ~ 50 -60 minutes during hydration and several hours for dehydration, regardless of temperature, suggesting that the kinetics were limited by gas exchange in the large furnace tubes. Figure 2a shows the measured isothermal equilibrium chemical strain corresponding to the $\sim 0 \rightarrow 1.06\%$ H_2O change as a function of composition. Data isotherms from

430 °C to 630 °C in 50 °C increments are plotted. It can be observed that with increasing Zr concentration (x), in general, the measured chemical strain increases monotonically and significantly at a given temperature. The data at 630 °C deviate slightly from this trend, with the strain minimum occurring at intermediate values of x rather than at x = 0 as for the other temperatures. For low values of x (x=0, x=0.3), the chemical strain also increases significantly with increasing temperature. For the x=1 composition, on the other hand, the chemical strain actually decreases slightly with increasing temperature, although the magnitude of that effect is not so large. The reasons for these differences will be explored in the discussion section.

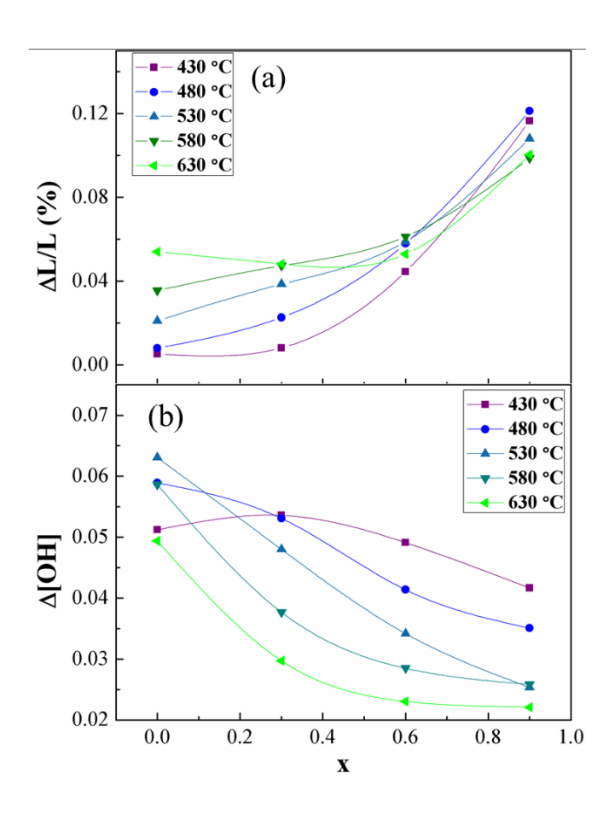


Figure 2. a) The chemical strain value as a function of Zr concentration (x) in $BaCe_{0.9-x}Zr_xY_{0.1}O_{3-\delta}$ and b) The change in $(OH)_O$ concentration per formula unit upon increasing pH_2O from ~ 0 to 1.06% as a function of Zr concentration (x) in $BaCe_{0.9-x}Zr_xY_{0.1}O_{3-\delta}$

Figure 2b shows the corresponding equilibrium change in $(OH)_0$ concentration per formula unit determined from the isothermal measured mass changes for $\sim 0 \rightarrow 1.06\%$ H₂O, using eq. 5, as a function of Zr concentration (x). Again, the data are plotted as isotherms from 430 to

630 °C in 50 °C increments. At all but the lowest temperature, the proton concentration change in the oxide decreases with increasing Zr concentration (x). The proton concentration change is also generally lower with increasing temperature. For the oxide compositions in this study, the theoretical maximum change in (OH)₀ concentration that would be associated with full hydration of a dry sample would be 0.1 per formula unit, based on the oxygen vacancy concentration being half that of the Y acceptor concentration and eq. 1. The changes shown in Figure 2b therefore indicate that the samples are not undergoing full hydration/dehydration in these conditions. This is an important point to note, as many studies assume that full hydration and dehydration occurs in estimating CCEs from XRD or dilatometric data in humid and dry conditions. As discussed in the introduction, such an approach could lead to underestimation of CCE values.

Figure 3a shows the CCE values derived from the data in Figure 2a-b, i.e., the chemical strain normalized to the proton concentration change per formula unit, as shown in eq. 3. Data are plotted vs. Zr concentration (x), again at temperature isotherms from 430-630 °C. In this temperature range, the CCE increases monotonically with increasing Zr concentration (x). This result follows clearly from the dilatometric and TGA results, as the chemical strain was generally larger for increasing x while the mass change was generally smaller. At each composition, the

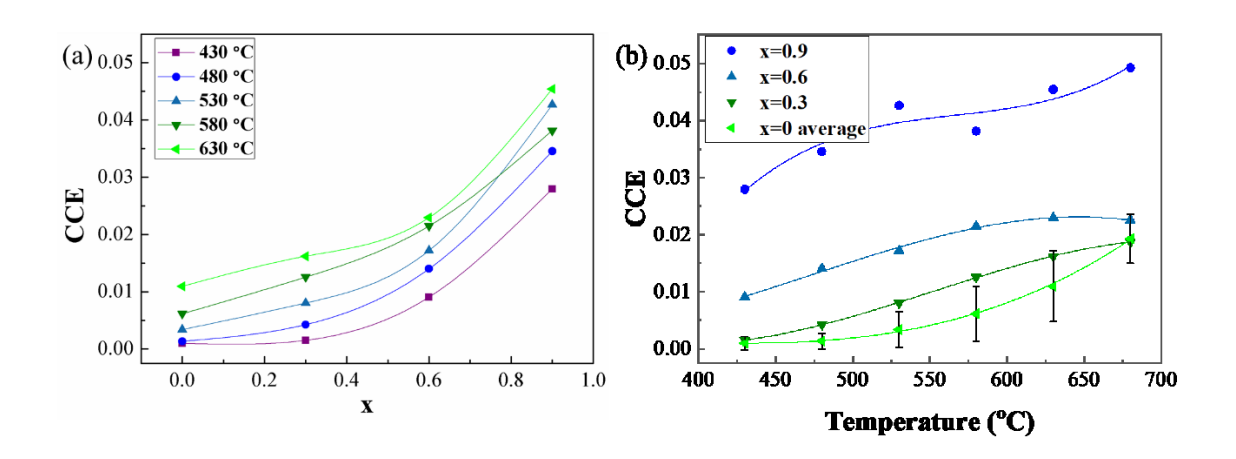


Figure 3. a) CCE as a function of Zr concentration (x) in $BaCe_{0.9-x}Zr_xY_{0.1}O_{3-\delta}$ and b) CCE as a function of measuring temperature for four compositions, labeled by x in $BaCe_{0.9-x}Zr_xY_{0.1}O_{3-\delta}$. The x=0 data are an average over multiple replicate samples with different densities and processing routes.

CCE also increases with increasing temperature. This result again follows straightforwardly from those in Figure 2a-b, particularly as the proton concentration change decreased with increasing temperature. The CCEs (same data) are also shown as a function of temperature in Figure 3b, where it can clearly be seen that the magnitude of the increase in CCE with temperature is relatively similar for all the compositions studied. Except for the x=0 composition, the temperature dependence of the CCE is roughly linear, as has been seen for perovskite compositions undergoing reduction-induced chemical expansion⁶¹. For the x=0 composition, a power law dependence is observed, as has been reported for redox-induced chemical expansion of a fluorite structured composition⁶².

In-situ, high temperature XRD (HTXRD) was employed to determine the degree of anisotropic expansion and the effect of symmetry changes upon heating in the least symmetric end-member, BaCe_{0.9}Y_{0.1}O_{3- δ}. Lattice parameters from refinement are shown in Figure 4. There is a phase transition from *Pnma* to *Imma* at 350° C, and the R $\bar{3}$ c phase begins to contribute to the refinement at 530° C, making up 10% and 33% of the sample at 530° and 630° C, respectively. From the refined lattice parameters, isothermal hydration strain along each axis is shown in Figure 5a, indicating that chemical strain appears to become significant at 430° C and above. Anisotropic expansion is clearly observed, as each axis exhibits distinguishable strain: above 430° C, the axis-resolved isothermal hydration strain is in the order b > c > a for the *Imma* phase. Quantitatively, the chemical strain anisotropy at 630° C is b/a = 2.6 and b/c = 1.7.

We had initially hypothesized that this unequal expansion behavior along each axis could be a key factor in the lower observed CCEs for the lower symmetry phases (lower x). As mentioned, one contributing reason could be that in randomly oriented, polycrystalline sintered samples, neighboring grains with different axis alignments could constrain one another during

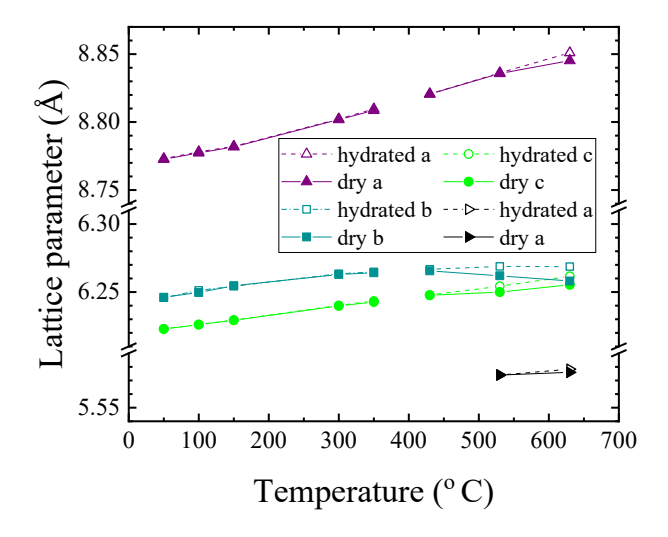


Figure 4. Lattice parameters for dry and hydrated $BaCe_{0.9}Y_{0.1}O_{3-\delta}$. Phases are $Pnma \le 350^{\circ}$ C, $Imma \ge 430^{\circ}$ C, and contributions from $R\overline{3}c \ge 530^{\circ}$ C (black).

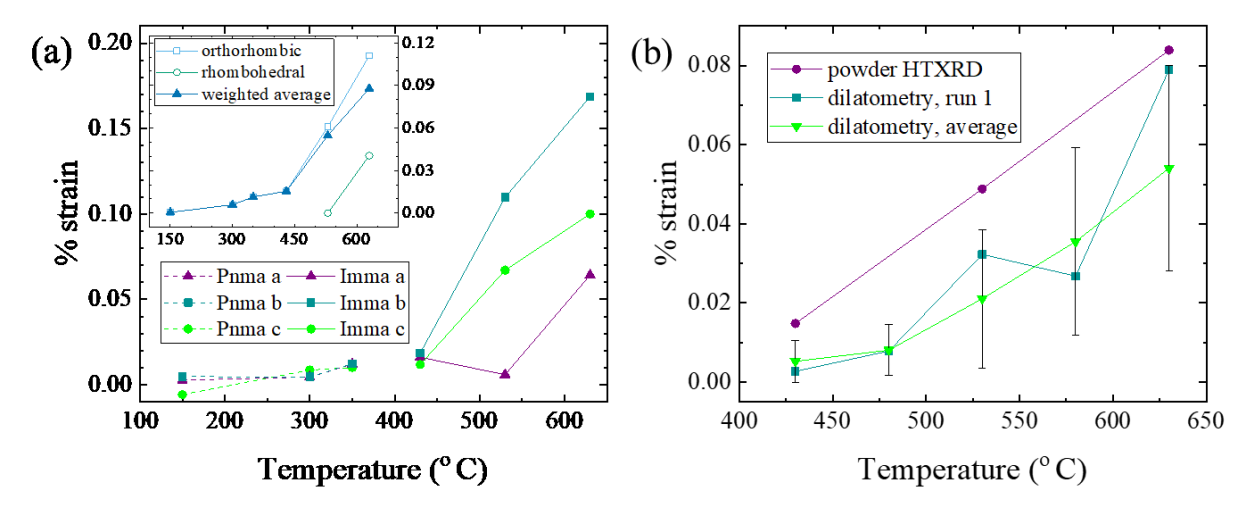


Figure 5. a) Isothermal hydration-induced strain calculated from the refined lattice parameters along each axis (reference points are dry condition at each temperature). The inset shows the linear isothermal hydration strain calculated from refined (unit cell volume)^{1/3} changes. The weighted average includes the contribution from orthorhombic and rhombohedral phases. b) Comparison of isothermal hydration strains measured by XRD and dilatometry for $BaCe_{0.9}Y_{0.1}O_3$.

 δ (reference points are dry condition for each temperature). The HTXRD data represent linearized average strains using a weighted average of the orthorhombic and rhombohedral phases present. "Run 1" refers to the first dilatometry sample of BaCe_{0.9}Y_{0.1}O_{3- δ}, which was also the sample run in the HTXRD measurement. "Average" refers to the average of all BaCe_{0.9}Y_{0.1}O_{3- δ} samples tested by dilatometry. Error bars represent the standard deviations from 3 dilatometry experiments on different samples run under the same conditions; uncertainty in strains from the XRD measurements are smaller than the data points.

expansion. To test this idea, the hydration strains of the x=0 composition were compared for unconstrained powder vs. bulk samples. Figure 5b shows the comparison between powder HTXRD and bulk dilatometric strains. The linearized strain for the case of the anisotropically expanding powder was calculated from the cube root of the unit cell volumetric strain, using the weighted average of orthorhombic and rhombohedral phase contributions. While both techniques reveal similar trends in isothermal hydration strain vs. temperature, the magnitude of the strains in powder HTXRD is higher for all temperatures, suggesting that the particles in the powder are able to expand more freely, relative to the sintered bars in dilatometry. On the other hand, Figure 5b shows that powder XRD strains are greater than those in dilatometry by, at most, a factor of ~2, whereas CCE values of cubic BaZr_{0.9}Y_{0.1}O_{3-δ} are greater than those of BaCe_{0.9}Y_{0.1}O_{3-δ} by a factor of 5 or more. This large change of CCE between the zirconate and cerate endmembers suggests that the microstructural effect of constraining anisotropically-expanding grains cannot be the only (or even primary) cause of lower CCE in the sintered Ce-containing compositions. Further, the

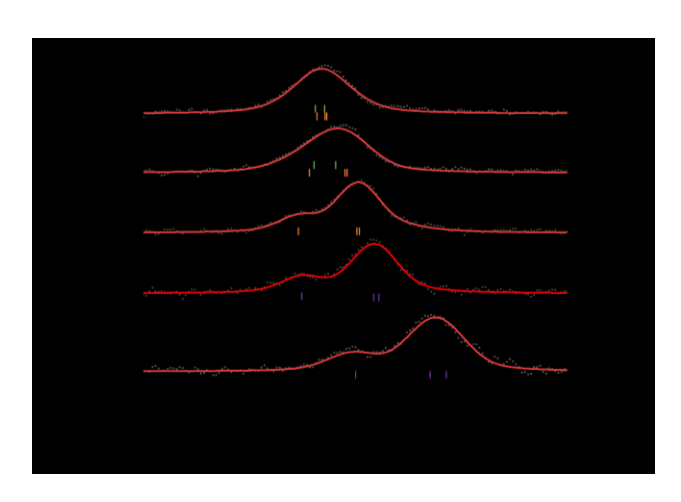


Figure 6. Change in peak shape illustrating the subtle move toward higher symmetry within a space group as temperature increases (Pnma: 25-350° C, Imma: 430-630° C). Black dots are raw data and red lines are the Rietveld refinements. $K\alpha_2$ contributions have been subtracted. Indices from left to right are, Pnma (purple) and Imma (orange): 040, 004, 422, and $R\overline{3}c$ (green): 422, 202.

similar and significant temperature dependence of powder XRD and bulk dilatometric isothermal chemical strain for the distorted structure of BaCe_{0.9}Y_{0.1}O_{3-δ} suggests an important role of a common underlying crystal chemical mechanism.

HTXRD also provided observations of subtle temperature-dependent symmetry changes that may aid interpretation of the temperature dependence of the isothermal hydration strain for BaCe_{0.9}Y_{0.1}O_{3-δ}. Although *Imma* is the dominant phase for 430°-630° C, the XRD results suggest that the structure exhibits a gradual change to higher symmetry as temperature increases within this range. This process can be seen by the convergence of b and c lattice parameters in Figure 4, and by the change in peak shape in Figure 6; two distinct peaks converge toward a single, broad peak as temperature increases, consistent with a transition from orthorhombic to rhombohedral symmetry. This observation of a gradual increase of symmetry with rising temperature in the distorted BaCe_{0.9}Y_{0.1}O_{3-δ} composition coincides with increasing macroscopic chemical strains and CCEs with rising temperature.

3.2. Computational

DFT simulations were performed to compare the structure, properties, and hydration-induced expansion behavior of the endmember x=0 (cerate) and x=0.9 (zirconate) compositions, using the structural symmetries experimentally determined by XRD at 25 °C. DFT lattice parameters were in good agreement with those found experimentally, as shown in Table 1.

The obtained structures of dry BCY, hydrated BCY, dry BZY, and hydrated BZY are shown in Figure 7a, Figure 7b, Figure 7c, and Figure 7d respectively. The dry structures contain one oxygen vacancy, while the hydrated structures contain two hydroxyl ions. Two Y dopants are close to each other, and the oxygen vacancy is located between two Y dopants for both systems in the dry state. The most stable structure of dry BZY found here is the same as that in a recent DFT result⁶³. For the hydrated structures shown in Figure 7b and d, it is found, in both BCY and BZY systems, that the stable proton sites are in close vicinity to the dopant because of strong trapping energies with respect to the nearby Y dopant⁶⁴. The proton in BCY forms hydrogen bonds (1.78 Å, see Figure 7b) with the oxygen ions belonging to two different, neighboring octahedra (inter-octahedral bonding), while the proton in BZY forms hydrogen bonds (1.65 Å, see Figure 7d) with the oxygen ions belonging to the same octahedron (intra-octahedral bonding). This difference is caused by the weaker oxygen-cerium bonds in BCY compared to stronger oxygen-zirconium bonds in BZY. The variation in bonding strength is also reflected in the bulk modulus values for these two systems, shown in Table 2, where the bulk modulus is ~33% larger for the zirconate endmember.

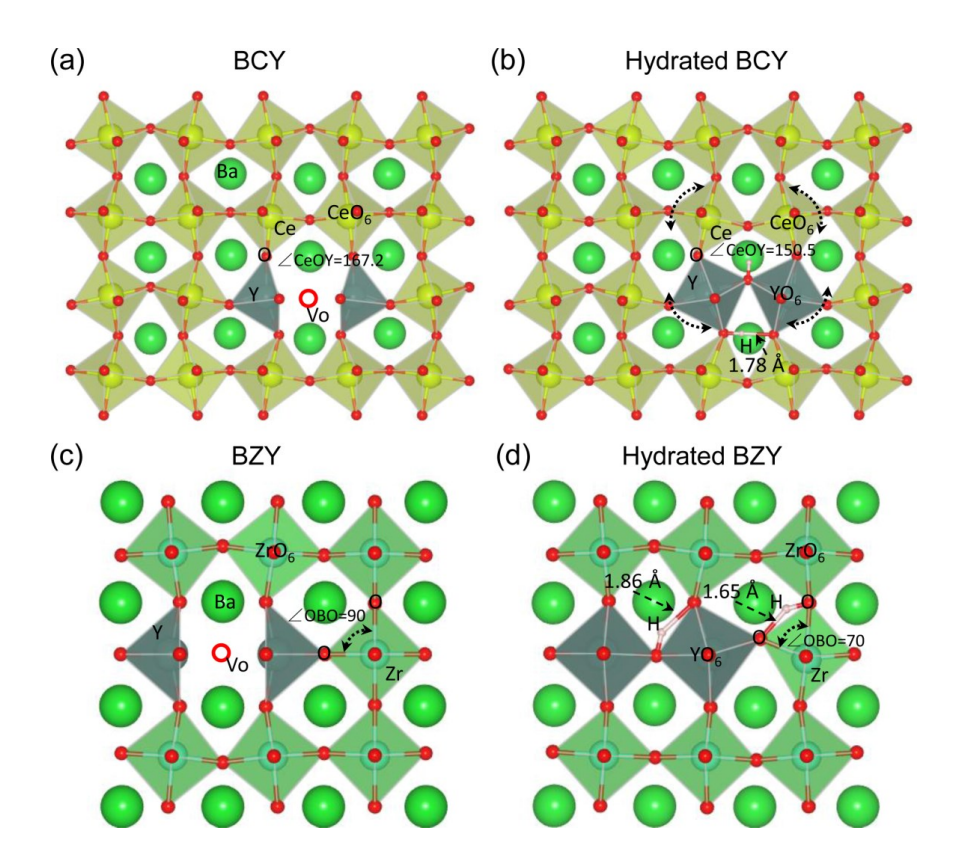


Figure 7. Optimized orthorhombic (a) BCY and (b) hydrated BCY systems, and cubic (c) BZY and (d) hydrated BZY systems. Ba, Zr, Ce, Y, O, and H ions are green, light blue, yellow, dark blue, red, and white, respectively, and red hollow circles represent oxygen vacancies.

Table 2. Selected calculated properties of $BaCe_{1-y}Y_yO_{3-\delta}$, and $BaZr_{1-y}Y_yO_{3-\delta}$, with previous theoretical and experimental hydration enthalpies shown for comparison

	у	$BaCe_{1-y}Y_yO_{3-\delta}$	$BaZr_{1-y}Y_yO_{3-\delta}$
Hydration enthalpy (eV) GGA-PBE (This work)	0.06-0.07	-1.36 (-1.38)	-0.52 (-0.53)
Hydration enthalpy (eV) GGA-PBE (Gd-BaCeO ₃) ⁶⁵	0.06-0.07	-1.34	
Hydration enthalpy (eV) Experiment ⁶⁶	0.1	-1.68	-0.78
Bulk modulus (GPa) DFT (This work)	0.06-0.07	105.9 (105.3) [dry] 106.9 (106.8) [hydrated]	141.1 (139.1) [dry] 140.5 (137.7) [hydrated]
Voronoi volume v ₀ vs O ₀ (Å ³), DFT (This work)	0.06-0.07	18.8 vs. 18.9	14.7 vs. 15.7

Note: Simulated values in round parentheses are for a less-stable dopant configuration with distant Y dopants rather than the more stable configuration of closely spaced Y dopants used for the majority of the data.

Moreover, the hydrogen bonds are formed in hydrated BCY through octahedral rotations, as shown in Figure 7b, where one of initial Ce-O-Y angles changes from 167.2° to 150.5°, while in hydrated BZY, the hydrogen bonds are formed by O-B-O bending motions as shown in Figure 7d, where one of the initial O-B-O angles is reduced from 90° to 70° degrees. In order to further verify the simulations of the hydration reaction, we calculated the hydration enthalpy at zero pressure and zero temperature based on the total energy of each system in the Kröger-Vink hydration notation: $\Delta E_{hyd} = E_{tot}(hydrated) - E_{tot}(V_0^{\bullet\bullet}) - E_{tot}(H_2O), \text{ where } E_{tot}(hydrated) \text{ is the total energy of the system containing two dopants and two protons, } E_{tot}(V_0^{\bullet\bullet}) \text{ is the total energy of an isolated water molecule}^{65,67}. The calculated hydration enthalpies for BCY and BZY are shown in Table 2. The hydration enthalpies are consistent with previous DFT calculations and experimental results}^{65,66}$

In order to address the chemical expansion, the energy as a function of volume for BCY vs. hydrated BCY and BZY vs. hydrated BZY was obtained, as shown in Figure 8. The data are fitted to a Birch-Murnaghan equation of state^{68,69}:

$$E(V) = E_0 + \frac{9V_0B_0}{16} \left\{ \left[\left(\frac{V_0}{V} \right)^{\frac{2}{3}} - 1 \right]^3 B_0 + \left[\left(\frac{V_0}{V} \right)^{\frac{2}{3}} - 1 \right]^2 \left[6 - 4 \left(\frac{V_0}{V} \right)^{\frac{2}{3}} \right] \right\}$$
 (6)

where E is the total energy, E_0 and V_0 are the equilibrium energy and volume, respectively, V is the deformed volume, B_0 is the bulk modulus, and B_0 ' is the derivative of the bulk modulus with respect to energy. Based on the calculated equilibrium volume and volume change, the chemical

expansion upon hydration is obtained for BCY and BZY. Since the change in proton concentration is dictated by the simulations, this approach also enables determination of the CCE, i.e., the expansion normalized to the defect concentration change. As shown in Table 1, the simulations yield a higher CCE at 0 K for BZY compared to BCY by more than a factor of 2, consistent with the experimental results. The simulated CCE for BZY is in good agreement with the experimentally measured value, while for BCY the simulated CCE at 0 K is higher than the experimentally determined value at intermediate temperatures. It should be noted that the DFT simulations incorporate crystal chemical effects, but not microstructural effects, so the qualitative agreement with the experimental trend suggests a crystal chemical contribution. Microstructural contributions were also studied and observed separately in the measurements, and those contributions, plus the change in crystal structure with temperature that is present for BCY but absent for BZY, may explain the difference in the measured vs. simulated BCY CCE values.

The bulk moduli agree with the previous experimental and computational results^{70–73}. In addition to the more stable configuration of two close Y dopants discussed here, both the BCY and BZY systems containing two distant Y dopants were also simulated, for comparison. The structures are not shown here for brevity. Some of the results for this less stable configuration with distant Y dopants are included in Table 1 and Table 2 in italics within round brackets. These results are included here, as other reports have raised the possibility of experimental samples with distant Y dopant ions.

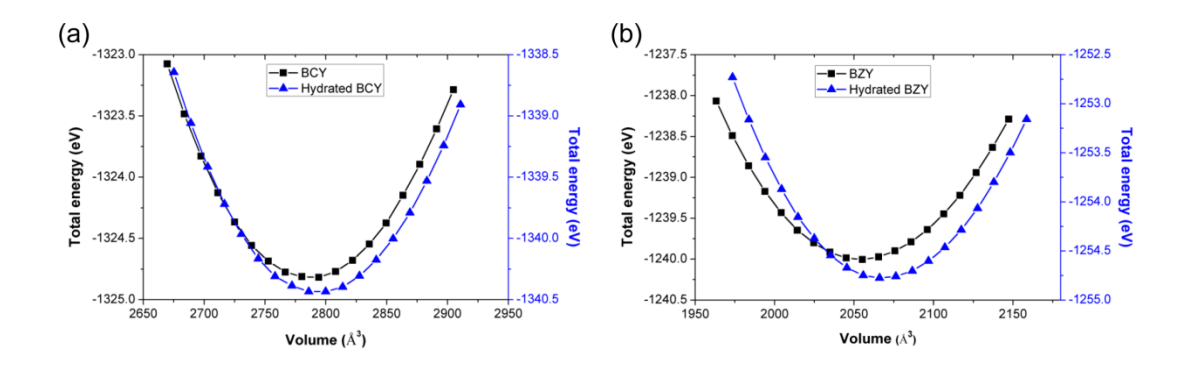


Figure 8. The total energy as a function of volume for (a) BCY and hydrated BCY, and (b) BZY and hydrated BZY.

Additional selected results of the calculations are shown in Table 2. The zirconate exhibited a smaller effective oxygen vacancy volume than the cerate. The oxygen vacancy was also smaller than the oxide ion in the zirconate. The cerate exhibited a larger effective oxygen vacancy size, and in that case, the oxygen vacancy was found to have the same size as the oxide ion. Considering equation 1, during hydration (without simultaneous redox processes), an oxygen vacancy is replaced by an (OH) defect, and an oxide ion is also replaced by an (OH) defect. Therefore, the effective size of the oxygen vacancy can play an important role in determining the extent of chemical strain or CCE.

4. DISCUSSION

4.1. Explanations for CCE Trends

The experimental and computational results are in agreement that the hydration CCE decreases with decreasing Zr concentration in the Y-doped BaCeO₃-BaZrO₃ solid solution across the temperature range studied. The results are consistent with our initial hypothesis that inducing distortions away from the perfect cubic perovskite structure would lower the CCE. We also have seen that there appear to be both crystal chemical and microstructural contributions to this trend

related to symmetry, from the DFT and *in situ* XRD results, respectively. However, the results have also revealed that there are multiple crystal chemical changes as the Ce:Zr ratio is altered, which go beyond our initial hypothesis about how symmetry/distortions might play a role in CCEs. To reiterate, we initially suggested that the distorted structures would accommodate compositional changes during hydration through changes in octahedral rotations/tilts, leading to some bonds lengthening and others shortening and an overall smaller volume change, compared to cubic structures. In this study, we found that many features changed when substituting Ce for Zr to lower the tolerance factor: symmetry, unit cell size, oxygen vacancy and oxide ion sizes, bulk moduli and bonding strengths, intra- vs. inter-octahedral hydrogen bonding, and method of proton incorporation (octahedral rotation vs. bond bending). These factors are summarized in Table 3.

Table 3. Summary of trends in the solid solution

Feature	Trend with increasing x in BaCe _{0.9-x} Zr _x Y _{0.1} O _{3-δ} (0 \leq x \leq 0.9)	
Tolerance factor	↑	
Crystal symmetry	↑	
Unit cell volume	↓	
B-O bond strength	↑ (Zr-O stronger than Ce-O)	
Bulk modulus	↑	
Method of proton incorporation	octahedral rotations → O-B-O bending	
H-bonding type	inter-octahedral → intra-octahedral	
Size ratio of oxygen vacancy: oxide ion	↓	
CCE	<u></u>	

Factors that are perhaps somewhat extraneous to our initial hypothesis regarding symmetry effects include the unit cell volume, bond strength and related bulk modulus, and the relative size of the oxygen vacancy. Each of these may have contributed to the CCE trend independently of symmetry. Intuitively, one may expect insertion of a given amount of H₂O into a smaller unit cell volume would give rise to a greater strain (since the volume change is normalized to the initial

volume), assuming consistent effective sizes for (OH)_O. The larger CCE for the smaller zirconates is consistent with that first-order expectation. Similarly, based on eq. 1, one expects smaller oxygen vacancies in the dehydrated structure to give rise to larger chemical strains as the vacancies are filled by hydroxyl ions, again assuming a constant effective size of (OH)_O. The relatively smaller oxygen vacancies in the zirconates are thus also consistent with their larger observed hydration CCEs. The expectation for impact of bulk modulus or bond strength on CCEs is not so straightforward, but it is clear from the present work that not only crystal symmetry but also bond strengths play a role in determining how chemical stress from hydration is accommodated at the unit cell scale and which bond angles change.

However, some of these features in Table 3 may be related to each other. For example, Bjørheim *et al.*'s²³ phonon calculations showed a correlation between cubic symmetry, less negative (more favorable) hydration entropies, larger "chemical expansion coefficient of oxygen vacancies" (i.e., larger relative difference of effective oxygen vacancy and oxide ion sizes), and thus larger hydration chemical expansion coefficients, albeit for limited compositions (cubic BaZrO₃ and BaSnO₃ vs. orthorhombic BaCeO₃, and SrZrO₃). They noted that the vibrational entropy contribution, particularly of the oxygen vacancies, dominated the compositional trend at finite temperatures, rather than the configurational entropy, which nonetheless has a more intuitive link to symmetry and unit cell volume via variable positional degeneracy of oxygen vacancies and protons. Less negative entropies (more favorable hydration) correlated to less negative enthalpies (less favorable hydration), and the authors hypothesized that both of these properties ultimately relate to bonding strengths of oxide ions and protons. A monotonic trend of less negative hydration entropy vs. increasing Zr content has also been observed for the solid solution in the present work⁵⁰. Thus indirect links between symmetry, relative oxygen vacancy size, bonding strengths,

and hydration CCE are possible via the thermodynamics of hydration. On the other hand, by changing compositions, a number of the factors in Table 3 can be de-coupled for more systematic studies and isolation of the effects of certain factors in future work.

4.2. Temperature Effects

Temperature dependent CCEs have been observed for a number of perovskites undergoing redox-induced chemical expansion^{44,74}; however, thermal trends for hydration CCEs have been less studied. Hydration CCEs increased with temperature across the conditions and composition range studied in the present work. The reasons for this trend remain relatively unexplored, but we note that in the cases of non-cubic perovskites, their symmetry tends to increase with rising temperature. This effect was demonstrated in the HTXRD results of the distorted BaCe_{0.9}Y_{0.1}O_{3-δ} endmember in the present work. As we have observed here a general correlation between increasing CCE and increasing symmetry, the temperature dependence of CCEs in BaCe_{0.9}Y_{0.1}O₃δ is consistent. For distorted BaCe_{0.9}Y_{0.1}O_{3-δ} even the isothermal chemical strains increased monotonically with rising temperature, despite the isothermal proton concentration change peaking at an intermediate temperature for that composition. The opposite temperature dependence of chemical strain was apparent in cubic BaZr_{0.9}Y_{0.1}O_{3-δ}, where isothermal hydration strain decreased with rising temperature, consistent with the trend in its proton concentration change. Nonetheless, the cubic BaZr_{0.9}Y_{0.1}O_{3-δ} composition did demonstrate a similar temperature dependence of overall CCE, which cannot be explained by an increase of symmetry with increasing temperature. Instead, a potential contribution may come (to all compositions) from the tendency toward defect dissociation with increasing temperature; trapping of oxygen vacancies and/or protons near Y dopants will likely lessen during heating, leading to non-negligible, and non-linear modifications in the CCEs. The role of temperature-dependent hydration entropy

contributions could also be considered²³. A less likely contribution is the role of thermal expansion. We have observed here larger hydration CCEs for smaller (room temperature) pseudo-cubic unit cell volumes, when the volume is tailored by Ce:Zr ratio. This correlation contrasts with the observed increasing CCE with rising temperature, considering thermal expansion. However the thermal expansion contribution to unit cell volume is relatively small compared to the effect of Ce:Zr exchange, and thus temperature dependent volume changes of the non-hydrated structures are perhaps negligible in influencing CCE. More work could be done to better clarify the underlying causes of temperature dependent CCEs for these proton conductors. We included data from 680 °C in Figure 3b. This temperature was omitted from most of our results presentation, as we wished to ensure dominance of eq. 1 as the hydration process being tested. We note that the trend of CCE vs. composition begins to blur at 680 °C with all 3 lower Zr content compositions (0 $\leq x \leq 0.6$) exhibiting similar CCEs. Temperature impacts not only crystal symmetry, but also increases the populations of electronic defects. Thus the redox chemical processes in eq. 2 may start to come in to play in determining CCEs at the higher temperatures. Depending on the orbitals involved in hosting electronic defects and their spatial extent (delocalization), the electronic defects can play a role in determining the chemical strains under conditions enabling redox^{27,61,75}.

4.3. Microstructure and Dopant Distribution Effects on CCE Variability

We minimized, as much as possible, variations in microstructure when comparing between compositions in the solid solution, by using samples with a very narrow distribution of relative densities, and eliminating any isolated samples with microcracks. (In fact, a review of studies of thermal expansion on porous materials suggests that the role of varying porosity on expansion coefficients may be negligible.⁴¹) Nonetheless, through replicate analysis, we have noted variability in the hydration strains of different samples (having a broader microstructure and

processing route range) of the anisotropically expanding cerate endmember, as indicated by error bars on the plots. We also observed a difference in chemical strain between bulk and powder samples (Fig. 8). These results are suggestive of an influence of microstructure (e.g., grain size), as hypothesized for lower symmetry structures, on the CCEs. The implication is that, outside of single crystal studies, a range of CCEs may be more descriptive of sintered, anisotropically expanding materials, with an as-yet-to-be-modeled dependence on microstructure. Furthermore, we suggest that variability in CCE for a given composition may also arise from the role of dopant distribution. The DFT simulations demonstrated that the lowest energy configuration kept the Y dopants proximal to each other, with strong trapping of the protons by the dopants. However, the actual dopant distribution in samples may, in general, depend on the processing route, in particular the sintering temperature and cooling rate after sintering, which may affect the "freezing in" temperature of cation distributions. The trapping of defects by dopants may also lessen with increasing measurement temperature. It is worthwhile to remember that this dopant-defect distribution affected the CCEs and other parameters in the DFT simulations (Tables 1-2) and may also have this effect experimentally. In the present work, through use of a consistent processing route, we endeavored to lessen variability in cation distribution among samples, but this effect should be considered, particularly when comparing among different studies and measurement temperatures.

5. CONCLUSIONS

Proton-conducting oxides enable the promising intermediate-temperature performance of protonic ceramic electrolysis/fuel cells, and their chemo-mechanical durability must be addressed to enable long device operating lifetimes. Isothermal macroscopic and axis-resolved chemical strains and associated quantified changes in proton changes in the BaCe_{0.9-x}Zr_xY_{0.1}O_{3- δ} ($0 \le x \le 1$)

0.9) solid solution under equilibrium conditions were measured and simulated, leading to precise determination of hydration CCEs and their trends. In the intermediate temperature range, the CCEs monotonically decrease with increasing Ce substitution for Zr. This trend is consistent with our initial hypothesis that decreased perovskite crystal symmetry, relative to cubic $Pm\bar{3}m$, would lead to decreased CCEs. The results support this hypothesis; the tailoring of tolerance factor does result in lower symmetries with increasing Ce content, and both crystal chemical and microstructural contributions expected from symmetry effects appear to be present, according to DFT simulations and X-ray diffraction and dilatometry of powder vs. bulk ceramic samples. Nonetheless, we observe that a number of other features systematically change across this solid solution, and some – like effective relative oxygen vacancy size and unit cell volume – are also clearly consistent with the observed CCE trend. Future work that decouples these features and isolates their effects will be beneficial for developing broadly applicable design principles. At this stage, we suggest that perovskite proton conductors with low symmetry, large oxygen vacancies, and large unit cells may exhibit low CCEs. For practical use, the Ce-rich compositions in the present study exhibit much lower hydration CCEs and lower chemical strains than the Zr-rich compositions in the conditions of this study and therefore likely greater macroscopic chemo-mechanical stability for implementation into intermediate temperature electrochemical energy devices. On the other hand, it should be noted that the lower symmetry of the Ce-rich compositions also gives rise to more anisotropic chemical (and thermal) expansion, which may lead to enhanced grain boundary stresses between differently oriented grains. The CCE trend should also be considered in the broader context of properties that vary with Zr:Ce ratio and tolerance factor in this solid solution, including stability in humid and CO₂-rich environments¹⁴, basicity, sintering characteristics^{10,11}, and transport behavior 12,13,15,16.

AUTHOR INFORMATION

Corresponding Author

*Corresponding author. Email: nhperry@illinois.edu

Present Addresses

T.C.: Toyota Motor Engineering & Manufacturing (China) Co., Ltd., 55 Dongsihuan Road,

Changshu, Jiangsu Province, 215542, China

Y.J.: Department of Astronautical Science and Mechanics, Harbin Institute of Technology,

Harbin, Heilongjiang 150001, P. R. China

N.A.: Oden Institute for Computational Engineering and Sciences, Walker Department of

Mechanical Engineering, The University of Texas at Austin, Austin, TX, 78705

Author Contributions

The manuscript was written through contributions of all authors. All authors have given approval

to the final version of the manuscript. §These authors contributed equally.

ACKNOWLEDGEMENTS

This work was supported financially by a NSF CAREER grant to NHP (DMR-1945482) and

initially by NSF grant no. 1545907 through a JSPS-NSF Partnership for International Research

and Education (PIRE). The use of facilities and instrumentation was supported by NSF through

the University of Illinois Materials Research Science and Engineering Center (DMR-1720633)

and by the Materials Research Laboratory Central Research Facilities. Authors acknowledge

support from the International Institute for Carbon Neutral Energy Research (WPI-I2CNER),

sponsored by the Japanese Ministry of Education, Culture, Sports, Science and Technology.

32

Computational work was performed using Blue Waters, which was provided by the University of Illinois and National Center for Supercomputing Applications supported by NSF awards OCI-0725070, ACI-1238993 and the state of Illinois.

REFERENCES

- (1) Kreuer, K. D. Proton-Conducting Oxides. *Annu. Rev. Mater. Res.* **2003**, *33*, 333–359. https://doi.org/10.1146/annurev.matsci.33.022802.091825.
- (2) Iwahara, H.; Asakura, Y.; Katahira, K.; Tanaka, M. Prospect of Hydrogen Technology Using Proton-Conducting Ceramics. *Solid State Ionics* 2004, 168 (3–4), 299–310. https://doi.org/10.1016/j.ssi.2003.03.001.
- (3) Fabbri, E.; Bi, L.; Tanaka, H.; Pergolesi, D.; Traversa, E. Chemically Stable Pr and y Co-Doped Barium Zirconate Electrolytes with High Proton Conductivity for Intermediate-Temperature Solid Oxide Fuel Cells. *Adv. Funct. Mater.* **2011**, *21* (1), 158–166. https://doi.org/10.1002/adfm.201001540.
- (4) Murakami, T.; Hester, J. R.; Yashima, M. High Proton Conductivity in Ba5Er2Al2ZrO13, a Hexagonal Perovskite-Related Oxide with Intrinsically Oxygen-Deficient Layers. *J. Am. Chem. Soc.* **2020**, *142* (27), 11653–11657. https://doi.org/10.1021/jacs.0c02403.
- (5) Rajendran, S.; Thangavel, N. K.; Ding, H.; Ding, Y.; Ding, D.; Reddy Arava, L. M. Tri-Doped BaCeO3-BaZrO3 as a Chemically Stable Electrolyte with High Proton-Conductivity for Intermediate Temperature Solid Oxide Electrolysis Cells (SOECs). ACS Appl. Mater. Interfaces 2020, 12 (34), 38275–38284. https://doi.org/10.1021/acsami.0c12532.

- (6) Montaleone, D.; Mercadelli, E.; Escolástico, S.; Gondolini, A.; Serra, J. M.; Sanson, A. All-Ceramic Asymmetric Membranes with Superior Hydrogen Permeation. *J. Mater. Chem. A* 2018, 6 (23), 15718–15727. https://doi.org/10.1039/c8ta04764b.
- (7) Yang, W.; Wang, L.; Li, Y.; Zhou, H.; He, Z.; Han, C.; Dai, L. An Easily Sintered, Chemically Stable Indium and Tin Co-Doped Barium Hafnate Electrolyte for Hydrogen Separation. J. Alloys Compd. 2021, 868, 159117. https://doi.org/10.1016/j.jallcom.2021.159117.
- (8) Kreuer, K. D. On the Development of Proton Conducting Materials for Technological Applications. *Solid State Ionics* **1997**, *97* (1–4), 1–15. https://doi.org/10.1016/s0167-2738(97)00082-9.
- (9) Hamakawa, S.; Hibino, T.; Iwahara, H. Electrochemical Hydrogen Permeation in a Proton-Hole Mixed Conductor and Its Application to a Membrane Reactor. *J. Electrochem. Soc.* 1994, 141 (7), 1720. https://doi.org/10.1149/1.2054993.
- (10) Park, J. S.; Lee, J. H.; Lee, H. W.; Kim, B. K. Low Temperature Sintering of BaZrO3-Based Proton Conductors for Intermediate Temperature Solid Oxide Fuel Cells. *Solid State Ionics* **2010**, *181* (3–4), 163–167. https://doi.org/10.1016/j.ssi.2009.06.015.
- (11) Yun, D. S.; Kim, J.; Kim, S. J.; Lee, J. H.; Kim, J. N.; Yoon, H. C.; Yu, J. H.; Kwak, M.; Yoon, H.; Cho, Y. et al. Structural and Electrochemical Properties of Dense Yttria-Doped Barium Zirconate Prepared by Solid-State Reactive Sintering. *Energies* 2018, 11 (11), 3083. https://doi.org/10.3390/en11113083.
- (12) Shirpour, M.; Merkle, R.; Lin, C. T.; Maier, J. Nonlinear Electrical Grain Boundary

- Properties in Proton Conducting Y-BaZrO3 Supporting the Space Charge Depletion Model. *Phys. Chem. Chem. Phys.* **2012**, *14* (2), 730–740. https://doi.org/10.1039/c1cp22487e.
- (13) Han, D.; Liu, X.; Bjørheim, T. S.; Uda, T. Yttrium-Doped Barium Zirconate-Cerate Solid Solution as Proton Conducting Electrolyte: Why Higher Cerium Concentration Leads to Better Performance for Fuel Cells and Electrolysis Cells. *Adv. Energy Mater.* **2021**, *11* (8), 2003149. https://doi.org/10.1002/AENM.202003149.
- (14) Bhide, S. V.; Virkar, A. V. Stability of AB 1 / 2 ′ B ″ 1 / 2 O 3 Type Mixed Perovskite Proton Conductors. J. Electrochem. Soc. 1999, 146 (12), 4386. https://doi.org/10.1149/1.1392648.
- (15) Lacz, A.; Grzesik, K.; Pasierb, P. Electrical Properties of BaCeO3-Based Composite Protonic Conductors. *J. Power Sources* **2015**, *279*, 80–87. https://doi.org/10.1016/j.jpowsour.2014.12.065.
- (16) Hibino, T.; Iwahara, H. CO2 Sensors Using BaCeO3-Based Ceramics. Sensors Actuators
 B. Chem. 1993, 13 (1-3), 483-485. https://doi.org/10.1016/0925-4005(93)85433-B.
- Wallis, J.; Urban, L.; Grimmer, C.; Bodnar, W.; Zimmermann, R.; Ricote, S.; Weltmann, K. D.; Burkel, E.; Kruth, A. Structural and Electrical Properties of BaZr0.7Ce0.2Y0.1O3–δ
 Proton Conducting Ceramic Fabricated by Spark Plasma Sintering. *Solid State Ionics* 2020, 345, 115118. https://doi.org/10.1016/j.ssi.2019.115118.
- (18) Peng, J.; Li, H.; Lin, S. Study on Properties of BaZr0.7Ce0.2Y0.1O3-δ Ceramics Prepared by High-Pressure Sintering. *J. Ceram. Soc. Japan* **2020**, *128* (2), 62–65. https://doi.org/10.2109/jcersj2.19186.

- (19) Poetzsch, D.; Merkle, R.; Maier, J. Proton Uptake in the H+ -SOFC Cathode Material Ba0.5Sr0.5Fe0.8Zn0.2O3-d: Transition from Hydration to Hydrogenation with Increasing Oxygen Partial Pressure. *Faraday Discuss.* **2015**, *182*, 129–143. https://doi.org/10.1039/c5fd00013k.
- (20) Tsidilkovski, V. I.; Putilov, L. P. The Role of Deep Acceptor Levels in Hydration and Transport Processes in BaZr1 XYxO3 δ and Related Materials. *J. Solid State Electrochem.* **2016**, *20* (3), 629–643. https://doi.org/10.1007/s10008-015-3087-1.
- (21) Hoedl, M. F.; Gryaznov, D.; Merkle, R.; Kotomin, E. A.; Maier, J. Interdependence of Oxygenation and Hydration in Mixed-Conducting (Ba,Sr)FeO 3–δ Perovskites Studied by Density Functional Theory. *J. Phys. Chem. C* 2020, 124, 11780–11789. https://doi.org/10.1021/acs.jpcc.0c01924.
- (22) Poetzsch, D.; Merkle, R.; Maier, J. Stoichiometry Variation in Materials with Three Mobile Carriers—Thermodynamics and Transport Kinetics Exemplified for Protons, Oxygen Vacancies, and Holes. *Adv. Funct. Mater.* **2015**, *25* (10), 1542–1557. https://doi.org/10.1002/ADFM.201402212.
- (23) Bjørheim, T. S.; Løken, A.; Haugsrud, R. On the Relationship between Chemical Expansion and Hydration Thermodynamics of Proton Conducting Perovskites. *J. Mater. Chem. A* **2016**, *4* (16), 5917–5924. https://doi.org/10.1039/c5ta10090a.
- (24) Torayev, A.; Sperrin, L.; Gomez, M. A.; Kattirtzi, J. A.; Merlet, C.; Grey, C. P. Local Distortions and Dynamics in Hydrated Y-Doped BaZrO3. *J. Phys. Chem. C* **2020**, *124* (30), 16689–16701. https://doi.org/10.1021/acs.jpcc.0c04594.

- (25) Chen, X.; Grande, T. Anisotropic Chemical Expansion of La1–XSrxCoO3–δ. *Chem. Mater.* 2013, 25 (6), 927–934. https://doi.org/10.1021/CM304040P.
- (26) Chen, X.; Grande, T. Anisotropic and Nonlinear Thermal and Chemical Expansion of La 1-XSrxFeO3-δ (x = 0.3, 0.4, 0.5) Perovskite Materials. *Chem. Mater.* **2013**, *25* (16), 3296–3306. https://doi.org/10.1021/cm401100c.
- (27) Perry, N. H.; Bishop, S. R.; Tuller, H. L. Tailoring Chemical Expansion by Controlling Charge Localization: In Situ X-Ray Diffraction and Dilatometric Study of (La,Sr)(Ga,Ni)O3-δ Perovskite. *J. Mater. Chem. A* **2014**, *2* (44), 18906–18916. https://doi.org/10.1039/c4ta02972k.
- (28) Brett, D. J. L.; Atkinson, A.; Brandon, N. P.; Skinner, S. J. Intermediate Temperature Solid Oxide Fuel Cells. *Chem. Soc. Rev.* **2008**, *37* (8), 1568–1578. https://doi.org/10.1039/b612060c.
- (29) Han, D.; Shinoda, K.; Sato, S.; Majima, M.; Uda, T. Correlation between Electroconductive and Structural Properties of Proton Conductive Acceptor-Doped Barium Zirconate. *J. Mater. Chem. A* **2015**, *3* (3), 1243–1250. https://doi.org/10.1039/c4ta05701e.
- (30) Kinyanjui, F. G.; Norberg, S. T.; Ahmed, I.; Eriksson, S. G.; Hull, S. In-Situ Conductivity and Hydration Studies of Proton Conductors Using Neutron Powder Diffraction. *Solid State Ionics* **2012**, *225*, 312–316. https://doi.org/10.1016/j.ssi.2012.05.018.
- (31) Andersson, A. K. E. E.; Selbach, S. M.; Knee, C. S.; Grande, T. Chemical Expansion Due to Hydration of Proton-Conducting Perovskite Oxide Ceramics. *J. Am. Ceram. Soc.* **2014**, 97 (8), 2654–2661. https://doi.org/10.1111/jace.12990.

- (32) Han, D.; Hatada, N.; Uda, T.; Koc, R. Chemical Expansion of Yttrium-Doped Barium Zirconate and Correlation with Proton Concentration and Conductivity. *J. Am. Ceram. Soc.* 2016, 99 (11), 3745–3753. https://doi.org/10.1111/jace.14377.
- (33) Mather, G. C.; Heras-Juaristi, G.; Ritter, C.; Fuentes, R. O.; Chinelatto, A. L.; Pérez-Coll, D.; Amador, U. Phase Transitions, Chemical Expansion, and Deuteron Sites in the BaZr0.7Ce0.2Y0.1O3-δ Proton Conductor. *Chem. Mater.* 2016, 28 (12), 4292–4299. https://doi.org/10.1021/acs.chemmater.6b01095.
- (34) Ricote, S.; Hudish, G.; O'Brien, J. R.; Perry, N. H. Non Stoichiometry and Lattice Expansion of BaZr0.9Dy0.1O3-δ in Oxidizing Atmospheres. *Solid State Ionics* **2019**, *330*, 33–39. https://doi.org/10.1016/j.ssi.2018.12.006.
- (35) Tarutina, L. R.; Vdovin, G. K.; Lyagaeva, J. G.; Medvedev, D. A. BaCe0.7– XZr0.2Y0.1FexO3–δ Derived from Proton-Conducting Electrolytes: A Way of Designing Chemically Compatible Cathodes for Solid Oxide Fuel Cells. *J. Alloys Compd.* **2020**, *831*, 154895. https://doi.org/10.1016/j.jallcom.2020.154895.
- (36) Sosnowska, I.; Przenioslo, R.; Schäfer, W.; Kockelmann, W.; Hempelmann, R.; Wysocki,
 K. Possible Deuterium Positions in the High-Temperature Deuterated Proton Conductor
 Ba3Ca1+yNb2-YO9-δ Studied by Neutron and X-Ray Powder Diffraction. *J. Alloys Compd.* 2001, 328 (1–2), 226–230. https://doi.org/10.1016/S0925-8388(01)01299-3.
- (37) Hudish, G.; Manerbino, A.; Coors, W. G.; Ricote, S. Chemical Expansion in $BaZr0.9-xCexY0.1O3-\delta$ (x=0 and 0.2) upon Hydration Determined by High-Temperature X-Ray Diffraction. *J. Am. Ceram. Soc.* **2018**, *101* (3), 1298–1309.

- https://doi.org/10.1111/jace.15275.
- (38) Sereda, V. V.; Tsvetkov, D. S.; Malyshkin, D. A.; Ivanov, I. L.; Sednev-Lugovets, A. L.; Zuev, A. Y. Hydration-Induced Chemical Expansion of BaCa(1+y)/3Nb(2-y)/3O3-δ·xH2O (BCN) and Other Proton-Conducting Perovskite Oxides. *Solid State Ionics* **2020**, *358*, 115516. https://doi.org/10.1016/j.ssi.2020.115516.
- (39) Fujisaki, T.; Staykov, A. T.; Jing, Y.; Leonard, K.; Aluru, N. R.; Matsumoto, H. Understanding the Effect of Ce and Zr on Chemical Expansion in Yttrium Doped Strontium Cerate and Zirconate by High Temperature X-Ray Analysis and Density Functional Theory. *Solid State Ionics* **2019**, *333*, 1–8. https://doi.org/10.1016/j.ssi.2019.01.009.
- (40) Tsidilkovski, V.; Kuzmin, A.; Putilov, L.; Balakireva, V. H/D Isotope Effect for Hydrogen Solubility in BaZr0.9Y0.1O3–δ: Chemical Expansion Studies. *Solid State Ionics* **2017**, *301*, 170–175. https://doi.org/10.1016/J.SSI.2017.01.028.
- (41) Løken, A.; Ricote, S.; Wachowski, S. Thermal and Chemical Expansion in Proton Ceramic Electrolytes and Compatible Electrodes. *Crystals* **2018**, *8* (9), 365. https://doi.org/10.3390/cryst8090365.
- (42) Yamaguchi, S.; Yamada, N. Thermal Lattice Expansion Behavior of Yb-Doped BaCeO3. Solid State Ionics 2003, 162–163, 23–29. https://doi.org/10.1016/S0167-2738(03)00249-2.
- (43) Anderson, L. O.; Yong, A. X. Bin; Ertekin, E.; Perry, N. H. Toward Zero-Strain Mixed Conductors: Anomalously Low Redox Coefficients of Chemical Expansion in Praseodymium-Oxide Perovskites. *Chem. Mater.* 2021, Article ASAP. https://doi.org/10.1021/ACS.CHEMMATER.1C02739.

- (44) Kim, C. S.; Perry, N. H.; Bishop, S. R.; Tuller, H. L. Electro-Chemo-Mechanical Studies of Perovskite-Structured Mixed Ionic-Electronic Conducting SrSn1-XFexO3-x/2+δ Part III: Thermal and Chemical Expansion. *J. Electroceramics 2018 404* **2018**, *40* (4), 332–337. https://doi.org/10.1007/S10832-018-0134-1.
- (45) Grande, T.; Tolchard, J. R.; Selbach, S. M. Anisotropic Thermal and Chemical Expansion in Sr-Substituted LaMnO 3+δ: Implications for Chemical Strain Relaxation. *Chem. Mater.* 2012, 24 (2), 338–345. https://doi.org/10.1021/cm2030608.
- (46) Leonard, K.; Lee, Y. S.; Okuyama, Y.; Miyazaki, K.; Matsumoto, H. Influence of Dopant Levels on the Hydration Properties of SZCY and BZCY Proton Conducting Ceramics for Hydrogen Production. *Int. J. Hydrogen Energy* 2017, 42 (7), 3926–3937. https://doi.org/10.1016/j.ijhydene.2016.10.120.
- (47) Shannon, R. D. Revised Effective Ionic Radii and Systematic Studies of Interatomic Distances in Halides and Chalcogenides. *Acta Crystallogr. Sect. A* **1976**, *32* (5), 751–767. https://doi.org/10.1107/S0567739476001551.
- (48) Goldschmidt, V. M. The Laws of Crystal Chemistry. *Naturwissenschaften* **1926**, *14* (21), 477–485.
- (49) He, T.; Kreuer, K. D.; Baikov, Y. M.; Maier, J. Impedance Spectroscopic Study of Thermodynamics and Kinetics of a Gd-Doped BaCeO3 Single Crystal. *Solid State Ionics* **1997**, *95* (3–4), 301–308. https://doi.org/10.1016/s0167-2738(96)00613-3.
- (50) Ricote, S.; Bonanos, N.; Caboche, G. Water Vapour Solubility and Conductivity Study of the Proton Conductor BaCe(0.9 x)ZrxY0.1O(3 δ). *Solid State Ionics* **2009**, *180* (14–16),

- 990–997. https://doi.org/10.1016/J.SSI.2009.03.016.
- (51) Kresse, G.; Furthmüller, J. Efficiency of Ab-Initio Total Energy Calculations for Metals and Semiconductors Using a Plane-Wave Basis Set. *Comput. Mater. Sci.* **1996**, *6* (1), 15–50. https://doi.org/10.1016/0927-0256(96)00008-0.
- (52) Kresse G.a Joubert, D. . From Ultrasoft Pseudopotentials to the Projector Augmented-Wave Method. Phys. Rev. B - Condens. Matter Mater. Phys. 1999, 59 (3), 1758. https://doi.org/https://doi.org/10.1103/PhysRevB.59.1758.
- (53) Kresse, G.; Furthmüller, J. Efficient Iterative Schemes for Ab Initio Total-Energy Calculations Using a Plane-Wave Basis Set. *Phys. Rev. B Condens. Matter Mater. Phys.* **1996**, *54* (16), 11169. https://doi.org/10.1103/PhysRevB.54.11169.
- (54) Perdew, J. P.; Burke, K.; Ernzerhof, M. Generalized Gradient Approximation Made Simple. *Phys. Rev. Lett.* **1996**, 77 (18), 3865. https://doi.org/10.1103/PhysRevLett.77.3865.
- (55) Swift, M.; Janotti, A.; Van De Walle, C. G. Small Polarons and Point Defects in Barium Cerate. *Phys. Rev. B Condens. Matter Mater. Phys.* **2015**, *92* (21), 214114. https://doi.org/10.1103/PhysRevB.92.214114.
- (56) Levin, I.; Amos, T. G.; Bell, S. M.; Farber, L.; Vanderah, T. A.; Roth, R. S.; Toby, B. H. Phase Equilibria, Crystal Structures, and Dielectric Anomaly in the BaZrO3-CaZrO3 System. J. Solid State Chem. 2003, 175 (2), 170–181. https://doi.org/10.1016/S0022-4596(03)00220-2.
- (57) Kreuer, K. D.; Schönherr, E.; Maier, J. Proton and Oxygen Diffusion in BaCeO3 Based

- Compounds: A Combined Thermal Gravimetric Analysis and Conductivity Study. *Solid State Ionics* **1994**, *70*, 278–284. https://doi.org/10.1016/0167-2738(94)90323-9.
- (58) Kim, G. R.; Seo, H. H.; Jo, J. M.; Shin, E. C.; Yu, J. H.; Lee, J. S. Moving Boundary Diffusion Problem for Hydration Kinetics Evidenced in Non-Monotonic Conductivity Relaxations of Proton Conducting Perovskites. *Solid State Ionics* 2015, 272, 60–73. https://doi.org/10.1016/j.ssi.2015.01.003.
- (59) Samborski, S.; Sadowski, T. Dynamic Fracture Toughness of Porous Ceramics. *J. Am. Ceram. Soc.* **2010**, *93* (11), 3607–3609. https://doi.org/10.1111/j.1551-2916.2010.04133.x.
- (60) Rice, R. W. Grain Size and Porosity Dependence of Ceramic Fracture Energy and Toughness at 22°C. *J. Mater. Sci.* **1996**, *31* (8), 1969–1983. https://doi.org/10.1007/BF00356616.
- (61) Perry, N. H.; Kim, J. J.; Bishop, S. R.; Tuller, H. L. Strongly Coupled Thermal and Chemical Expansion in the Perovskite Oxide System Sr(Ti,Fe)O3-α. *J. Mater. Chem. A* **2015**, *3* (7), 3602–3611. https://doi.org/10.1039/c4ta05247a.
- (62) Omar, S.; Nino, J. C. Consistency in the Chemical Expansion of Fluorites: A Thermal Revision of the Doped Ceria. *Acta Mater.* **2013**, *61* (14), 5406–5413. https://doi.org/10.1016/j.actamat.2013.05.029.
- (63) Takahashi, H.; Yashima, I.; Amezawa, K.; Eguchi, K.; Matsumoto, H.; Takamura, H.; Yamaguchi, S. First-Principles Calculations for the Energetics of the Hydration Reaction of Acceptor-Doped BaZrO3. *Chem. Mater.* 2017, 29 (4), 1518–1526. https://doi.org/10.1021/acs.chemmater.6b03907.

- Yamazaki, Y.; Blanc, F.; Okuyama, Y.; Buannic, L.; Lucio-Vega, J. C.; Grey, C. P.; Haile,
 S. M. Proton Trapping in Yttrium-Doped Barium Zirconate. *Nat. Mater.* 2013, *12* (7), 647–651. https://doi.org/10.1038/nmat3638.
- (65) Bjørheim, T. S.; Kuwabara, A.; Ahmed, I.; Haugsrud, R.; Stølen, S.; Norby, T. A Combined Conductivity and DFT Study of Protons in PbZrO3 and Alkaline Earth Zirconate Perovskites. *Solid State Ionics* **2010**, *181* (3–4), 130–137. https://doi.org/10.1016/j.ssi.2009.04.013.
- (66) Kreuer, K. D. Aspects of the Formation and Mobility of Protonic Charge Carriers and the Stability of Perovskite-Type Oxides. *Solid State Ionics* 1999, 125 (1–4), 285–302. https://doi.org/10.1016/S0167-2738(99)00188-5.
- (67) Hermet, J.; Bottin, F.; Dezanneau, G.; Geneste, G. Thermodynamics of Hydration and Oxidation in the Proton Conductor Gd-Doped Barium Cerate from Density Functional Theory Calculations. *Phys. Rev. B - Condens. Matter Mater. Phys.* 2012, 85 (20), 205137. https://doi.org/10.1103/PhysRevB.85.205137.
- (68) Birch, F. Finite Elastic Strain of Cubic Crystals. *Phys. Rev.* **1947**, 71 (11), 809. https://doi.org/10.1103/PhysRev.71.809.
- (69) Murnaghan, F. D. The Compressibility of Media under Extreme Pressures. *Proc. Natl. Acad. Sci.* **1944**, *30* (9), 244. https://doi.org/10.1073/pnas.30.9.244.
- (70) Zhang, J.; Zhao, Y.; Xu, H.; Li, B.; Weidner, D. J.; Navrotsky, A. Elastic Properties of Yttrium-Doped BaCeO3 Perovskite. *Appl. Phys. Lett.* **2007**, *90* (16), 161903. https://doi.org/10.1063/1.2723679.

- Yamanaka, S.; Fujikane, M.; Hamaguchi, T.; Muta, H.; Oyama, T.; Matsuda, T.; Kobayashi,
 S. I.; Kurosaki, K. Thermophysical Properties of BaZrO3 and BaCeO3. *J. Alloys Compd.*2003, 359 (1–2), 109–113. https://doi.org/10.1016/S0925-8388(03)00214-7.
- (72) Goretta, K. C.; Park, E. T.; Koritala, R. E.; Cuber, M. M.; Pascual, E. A.; Chen, N.; De Arellano-Löpez, A. R.; Routbort, J. L. Thermomechanical Response of Polycrystalline BaZrO3. *Phys. C Supercond. its Appl.* **1998**, *309* (3–4), 245–250. https://doi.org/10.1016/S0921-4534(98)00588-7.
- (73) Malagoli, M.; Liu, M. L.; Park, H. C.; Bongiorno, A. Protons Crossing Triple Phase Boundaries Based on a Metal Catalyst, Pd or Ni, and Barium Zirconate. *Phys. Chem. Chem. Phys.* **2013**, *15* (30), 12525–12529. https://doi.org/10.1039/c3cp51863a.
- (74) Perry, N. H.; Marrocchelli, D.; Bishop, S. R.; Tuller, H. L. (Invited) Understanding and Controlling Chemo-Mechanical Coupling in Perovskite Oxides. *ECS Trans.* **2016**, *71* (24), 1. https://doi.org/10.1149/07224.0001ecst.
- (75) Marrocchelli, D.; Bishop, S. R.; Tuller, H. L.; Watson, G. W.; Yildiz, B. Charge Localization Increases Chemical Expansion in Cerium-Based Oxides. *Phys. Chem. Chem. Phys.* **2012**, *14* (35), 12070–12074. https://doi.org/10.1039/c2cp40754j.

TABLE OF CONTENTS GRAPHIC

